

Article

# MW-Scale High-Voltage Direct-Current Power Conversion for Large-Spacecraft Electric Propulsion

Ghazaleh Sarfi and Omid Beik \* 

Department of Electrical Engineering, Colorado School of Mines, Golden, CO 80401, USA;  
ghazaleh\_sarfi@mines.edu

\* Correspondence: beik@mines.edu

**Abstract:** This paper proposes a megawatt (MW)-scale high-voltage (HV) electrical power-conversion element for large-spacecraft electric propulsion (EP) systems. The proposed scheme is intended for long-term and crewed missions, and it is driven by a nuclear electric propulsion (NEP) that acts as a heat source. The scheme includes (i) A two-rotor generator (TRG), (ii) A rectification stage, and (iii) An isolated dual output DC-DC (iDC2) converter. The TRG is a high-reliability electric machine with two rotors, a permanent magnet rotor (PMR), and a wound field rotor (WFR). The PMR has a fixed flux and hence back-EMF, while the back-EMF due to the WFR is controlled by injecting a direct current (DC) into the WFR winding. The total TRG output voltage, which is the sum of voltages due to the PMR and WFR, is controlled over a prescribed region of spacecraft operation. The output of the TRG is rectified and connected to the input of the iDC2 converter. The iDC2 converter uses a three-winding transformer, where the primary winding is fed from the rectified output of TRG, the secondary winding processes the propulsion power to an electric thruster via a high-voltage DC (HVDC) link and a tertiary winding that is connected to the spacecraft's low-voltage DC (LVDC) power system. Three controllers are proposed for the system: an HVDC voltage controller, an HVDC current controller that controls the voltage and current processed to the thruster, and an LVDC controller that adjusts the current to the LVDC system. Detailed analytical models for the TRG, iDC2 converter, and controllers are developed and verified via simulations under different conditions. The analytical studies are further validated via results from a laboratory prototype.

**Keywords:** two-rotor generator; electric propulsion system; electric thruster; isolated DC-DC converter; spacecraft power system; spacecraft propulsion



**Citation:** Sarfi, G.; Beik, O. MW-Scale High-Voltage Direct-Current Power Conversion for Large-Spacecraft Electric Propulsion. *Electronics* **2024**, *13*, 1455. <https://doi.org/10.3390/electronics13081455>

Academic Editor: Ahmed Abu-Siada

Received: 23 February 2024

Revised: 2 April 2024

Accepted: 9 April 2024

Published: 11 April 2024



**Copyright:** © 2024 by the authors. Licensee MDPI, Basel, Switzerland. This article is an open access article distributed under the terms and conditions of the Creative Commons Attribution (CC BY) license (<https://creativecommons.org/licenses/by/4.0/>).

## 1. Introduction

Megawatt (MW)-scale electric propulsion (EP) systems for in-space applications have recently gained attention due to their viability for long-term and crewed missions such as interplanetary transport [1,2]. In-space EP systems use the electrical power generated by a source to produce thrust for propelling a spacecraft, usually via an electric thruster. Different EP thrusters for small spacecraft have been compared in [3], which are categorized as (i) electrothermal acceleration, such as resistojets [4] and arcjets [5]; (ii) electrostatic acceleration, such as ion thrusters [6] and Hall thrusters [7]; (iii) and electromagnetic acceleration, such as pulsed plasma thrusters (PPTs) [8] and vacuum arc thrusters (VATs) [9]. The sources of power in EP systems with thrusters up to a few tens of kilowatts (kW) are usually solar photovoltaic (PV) [10], batteries [2], and radioisotope thermoelectric generators (RTGs) [11]. However, scaling these sources for MW-scale propulsion is challenging.

Figure 1a shows a paradigm of spacecraft propulsion power comparing different energy sources based on mission duration. For short-term missions from weeks to months, batteries, solar PV batteries, chemical-based sources, and in some cases, fuel cells may be used. The DART spacecraft that was designed to collide with an asteroid to change its orbit in 2022 had a mission duration of 10 months with a power of 6.6 kW with two propulsion

sources: a solar PV source to generate electrical power for a NEXT-C electric thruster, and a chemical propulsion for hydrazine thrusters [12]. As seen in Figure 1a, for missions that take months to years, RTGs are used for low-power propulsion, and depending on the sun’s reach, solar PV batteries, sometimes referred to as solar electric propulsion (SEP), are used for power from tens of kW to few hundred kW. Voyager probes—the only spacecraft ever to operate outside the heliosphere—use RTGs rated at 500 W at the time of launch [13]. For MW-scale propulsions, two energy sources are viable options, as seen from Figure 1a: (i) chemical-based sources for short- to mid-term missions, and (ii) heat-based (i.e., nuclear) sources for mid- to long-term missions. One such mission is NASA’s Human Mars Exploration program, where nuclear thermal propulsion (NTP) and nuclear electric propulsion (NEP) are considered viable MW-scale propulsion solutions [14,15]. The design path for this mission is shown in Figure 1b. A planned mission lasts around 2 years, with a short stay (1 month) on Mars. The mission has separate cargo and crewed vehicles, with an assembly orbit in low Earth orbit (LEO) or cislunar space. For a spacecraft in this mission, NEP and NTP provide the low-thrust push for most of the mission, while chemical propulsion, e.g., based on liquid oxygen/methane, provides high thrust for maneuvers near Earth/Mars. The authors in [15] discuss cryogenic fluid management for such a mission. An overview of NTPs for Mars travel vehicles is provided in [16], while the authors in [17,18] compare the performance of different NTP engines for lunar and Mars applications. The work in [19] demonstrated that while using NTP (specific impulse 900 s) and NEP (specific impulse of 6000 s), there is significant LEO mass reduction compared to chemical propulsion (specific impulse of 440 s).

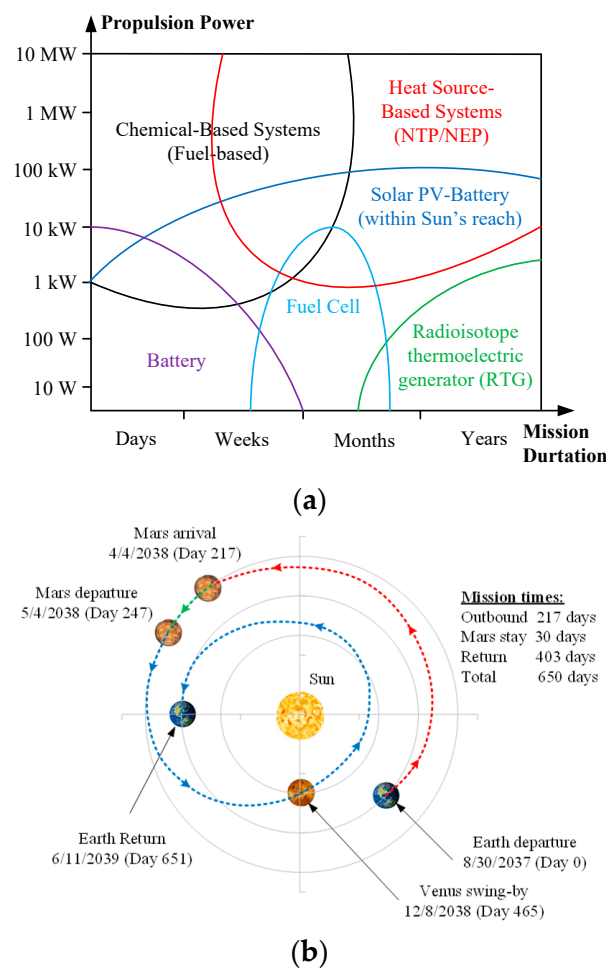


**Figure 1.** Spacecraft power and Mars travel path: (a) Paradigm of spacecraft propulsion power vs. mission duration.; (b) Mars travel design path.

A multi-MW NEP is discussed in [20] with a focus on mass reduction, while the work in [21–23] studied the possibility of NEPs combined with a chemical propulsion stage for human Mars-mission spacecraft. State-of-the-art NEPs and NTPs have recently been reviewed by NASA Engineering and Safety Center [24] and the National Academies of Science, Engineering, and Medicine [25], both of which indicated the need for research development to reach Technology Readiness Level 5 (TRL 5) to evaluate the suitability of NEP/NTP for human Mars missions [14]. The authors in [26] summarize key findings of NASA's space nuclear propulsion project regarding technology maturation for MW-class NEPs, where five critical technology elements for an NEP are defined: (i) nuclear reactor as the power source; (ii) power conversion, which includes converting the heat from the nuclear source to electrical power and includes a heat cycle such as the Brayton cycle connected to a turbine; (iii) power management and distribution (PMAD), which takes the electrical power from the power-conversion element and controls, then manages and processes it to a thruster and the spacecraft power system, whose main components are an electric generator and power electronics interface; (iv) electric propulsion subsystem (i.e., thruster); and (v) primary heat rejection system. The studies in [27–32] suggest a closed-cycle Brayton system for the NEP power-conversion element that spins a rotating electric generator, sometimes referred to as an alternator. The key performance parameters for an NEP power-conversion element suitable for the human Mars spacecraft reported in [14,26] are a mass-to-power ratio between 13 and 24 kg/kWe, power levels of 0.5 MW–4 MW, a voltage level of 1 kV, and a switching frequency of around 2–3 kHz for the power electronics switches. Of note, the power-conversion system within the NEP, i.e., the Brayton cycle and turbine, provides a limited range of speed for the electric generator, while the generator's output power depends on the electric thruster demand. For the overall control of the propulsion system, the generator's desired speed is controlled by the NEP, while sudden changes, which may occur due to changes in the electric thruster demand, are controlled by the PMAD, particularly by the power electronics interface (explained in more detail in Section 2). The sudden changes that may affect the generator's frequency in a very short period, such as the loss of a phase, may be controlled by a speed/frequency controller [14,33–35].

The NEP power-conversion element studies in the literature mainly focus on the prime mover aspects, i.e., the Brayton cycle [14,27–37]. The existing literature on MW-scale EP systems for spacecraft mainly focuses on the heat-source side, i.e., the nuclear reactor and power-conversion element, while there is limited literature on MW-scale high-voltage PMADs. Therefore, this paper is focused on the generator and control of the power processed to the PMAD. Specifically, in this paper, an electrical generation scheme is proposed that includes an MW-scale two-rotor generator, a rectifier, and a novel high-voltage (HV) isolated DC-DC converter with dual output that is responsible for the generation, control, and processing of the power to a common high-voltage DC (HVDC) bus for the thruster and spacecraft low-voltage DC (LVDC) power system. This work introduces a new converter circuitry (iDC2) design and utilizes its mathematical model to develop appropriate controllers tailored for MW-scale EP systems. A similar effort undertaken by NASA [38] involves the development of a converter based on a dual active bridge. Compared with the dual active bridge, the iDC2 converter offers a reduced component count, reduced losses, increased reliability (the number of active elements in iDC2 is 2, while this is 12 for the dual active bridge), and reduced cost [38]. The paper is organized as follows: The introduction and literature review are provided in Section 1. Section 2 discusses the proposed in-space electric propulsion system. In Section 3, design considerations and controllers are addressed. Simulation analyses are presented in Section 4, while the conclusions are provided in Section 5.

## 2. Proposed In-Space Electric Propulsion Scheme

Figure 2 shows the architecture of the proposed EP scheme, where a heat source (combined NEP reactor, Brayton cycle, and turbine) acts as a prime mover rotating at a

fixed speed and spinning a nine-phase two-rotor generator (TRG) whose output is rectified using a nine-phase bridge rectifier. The rectified voltage is then connected to the spacecraft HVDC bus using an isolated dual output DC-DC (iDC2) converter. The thermal energy released from a nuclear reactor is converted into electrical power for propulsion and the spacecraft power system. In this system, the reactor heat exchanger transfers heat from the reactor to a working fluid circulating in the cycle, while the turbine extracts mechanical work from the expanding fluid. The recuperator recovers waste heat from the turbine exhaust to preheat compressed air before combustion, enhancing overall efficiency. Subsequently, the radiator heat exchanger dissipates excess heat from the working fluid, ensuring optimal operating conditions. The compressor pressurizes the working fluid, and both the turbine and compressor are typically located on the same shaft, facilitating efficient energy transfer. Together, these elements enable the NEP Brayton cycle to convert thermal energy, produced by the nuclear reactor into mechanical power, which is then transferred to the TRG by being located on the same shaft as the turbine [32]. The electric thrusters typically necessitate DC input voltage for operation, as their internal mechanisms, such as electrodes and ionization chambers, depend on a consistent polarity of the electric field [38]. While spacecraft may generate AC power from sources, this must be converted to DC prior to being used by the electric thruster. Therefore, having a PMAD system capable of providing the required input voltage becomes crucial. For the Human Mars Exploration program, with an MW-class NEP system, voltages beyond 800 V [39] and 1000 V [35] are required by the electric thruster. Therefore, for this study, we selected a 1000 V HVDC bus system to connect with the electric thruster, which will be regulated by iDC2 to ensure stability and consistency. As for the loads connected to the LVDC bus, including various electronic devices such as communication systems, instruments, and actuators, the recommended DC voltage, as per [40,41], will be 200 V, which aligns with the choice made by this study. Note that the design of the LVDC and the spacecraft power system are beyond the scope of this study; the focus of this study will be on PMAD, with particular emphasis on the iDC2 converter design and control.

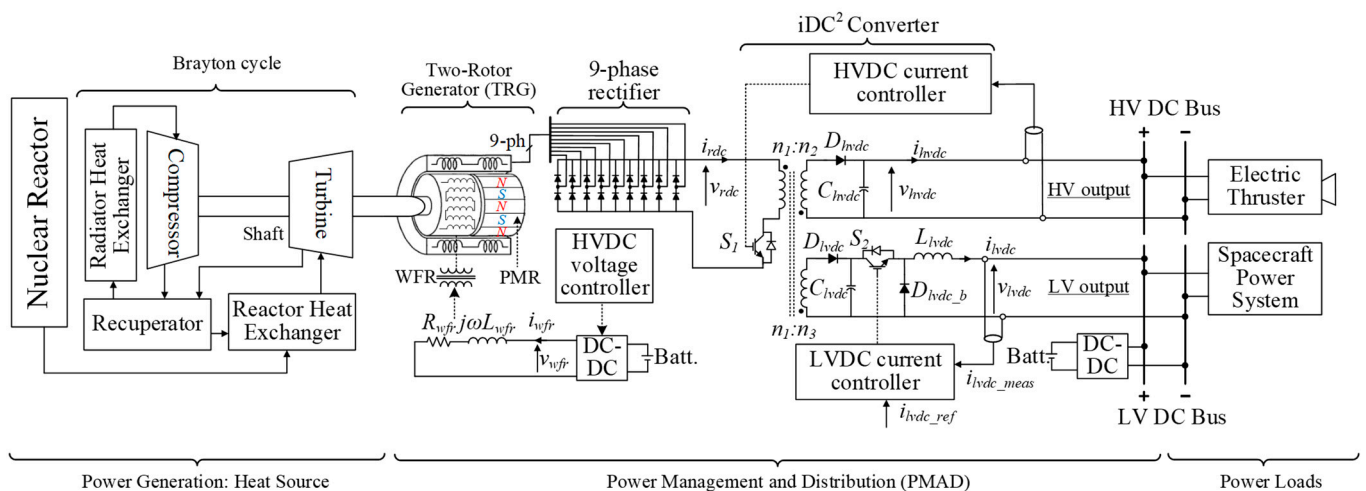


Figure 2. Architecture of proposed EP system.

In the context of PMAD, the TRG has two rotors: a permanent magnet rotor (PMR) and a wound field rotor (WFR). Both rotors are mounted on the same shaft, rotate at the same speed, and share the same stator. The PMR has a fixed magnetic flux; hence, at a fixed speed, it induces a fixed stator back-EMF. The flux due to the WFR is adjustable by controlling a DC current ( $i_{wfr}$ ) injected into the WFR winding; therefore, the back-EMF induced by the WFR is controlled. The TRG total back-EMF is the sum of induced voltages due to the PMR and WFR; thus, it is controlled over a prescribed region. Once launched (from the Earth), the spacecraft moves through different orbits until it descends to its destination, e.g., Mars. During this travel, the propulsion power varies, i.e., during orbit change, the electric

thruster requires the maximum power, while once it is put into orbit, the propulsion power is minimal to maintain the spacecraft's orbit. Therefore, the control for the WFR and the iDC2 converter will depend on the region of the operation for the spacecraft.

The PMR is the main rotor; it is designed to contribute 70% of the output due to its higher power density compared to the WFR part [42,43]. However, the WFR provides a controlled magnetic field with boosting and bucking functionality for the TRG; hence, it controls the TRG's rectified output voltage and consequently the spacecraft HVDC voltage. In the case of reduced magnetic field (e.g., due to demagnetized/damaged PMs from a reverse current), a positive DC current is injected to the WFR to boost the magnetic field and hence increase the TRG's output voltage. Similarly, in case of over-voltage (e.g., due to transients), a negative DC current is injected to the WFR winding to reduce the net magnetic field and hence output voltage. Therefore, the WFR provides active control over the TRG's output voltage, and hence power as the spacecraft power requirements varies during the mission. This is an additional degree of control in case the power electronics controls, i.e., iDC2 converter control, fail, hence increasing propulsion system reliability. In terms of multiphase winding, compared to three-phase systems, multiphase (greater than three phases) winding provides several benefits [44,45]. Fault tolerance is an inherent feature of multiphase systems. If one phase is failed (e.g., shorted), to maintain the same power in a three-phase system, the remaining two phases are overloaded by 50%, while in a nine-phase system, the remaining eight phases will be overloaded by 12.5%. To prevent the TRG from shutting down due to overload, the load will need to be reduced by 33% in a three-phase system; however, in a nine-phase system, the load will only need to be decreased by 11%. Therefore, compared to the three-phase system, a nine-phase TRG provides greater fault tolerance, reliability, and energy accessibility for the EP system. The nine-phase winding results in higher back-EMF (by 4.2%) [45] compared to three-phase winding due to an improved winding factor [46–49]. Therefore, for the same load, the nine-phase winding results in improved power density and efficiency not only for the TRG but also for the bridge rectifier and iDC2 converter, as the increased back-EMF results in a lower TRG phase current. Of note, the design of the TRG is out of the scope of this paper, but different aspects of the TRG, including its design, multiphase winding, and operation, have been addressed by the authors in [43,44].

The nine-phase TRG terminal is connected to a bridge rectifier in the proposed scheme, as seen in Figure 2. The rectified voltage at the output of an  $n$ -phase ( $n$ -leg) rectifier is expressed in (1) [49], and as seen, it has a linear relationship with the TRG back-EMF; therefore, it is controlled by the DC current injected into the WFR winding. This allows for the bridge rectifier to use passive diodes, rather than active switches (IGBTs/MOSFETs), which results in increased reliability as active switches contribute to 34% of power-electronics converter failures [50].

$$v_{rdc} = \frac{2n}{\pi} \sin\left(\frac{\pi}{n}\right) \hat{e}_{trg\_ph} + \Delta v_{rdcr} \quad (1)$$

where  $\hat{e}_{trg\_ph}$  is the TRG peak phase voltage, and  $\Delta v_{rdcr}$  is the voltage ripple. Note that the first term on the right side of (1) calculates the average rectified DC voltage for a pure sine wave. The second term is added to take into account the DC voltage ripple. The nine-phase voltage results in reduced DC ripples compared to the three-phase voltage, hence requiring smaller capacitive filtering elements at the output of the bridge rectifier. This increases the reliability of the system, as capacitors are a major reliability issue contributing to 20% of power-electronics converter failures [50].

The iDC2 converter, which is the core of this paper, is responsible for controlling and maintaining the desired output voltage and current while enabling the use of a passive rectification stage in lieu of an active converter at the output of the TRG. Eliminating the active rectifier enhances the reliability of the system and improves short-circuit current considerations that are common in active rectifiers [51]. The iDC2 is a high-voltage multiport DC-DC converter that meets the specific requirements of the proposed MW-scale propulsion system, and compared to other options that may be used in the proposed

scheme, such as single active bridge (SAB) or dual active bridge (DAB), offers (i) simplified circuit topology; (ii) a simple and robust control strategy that both enhances system responsiveness to dynamic changes and provides a dual-loop control for current and voltage; (iii) competitive cost; (iv) reduced component counts—in particular, the number of active switches in a DAB is 12, while this is 2 for the iDC2, which significantly improves the reliability of the conversion system as power electronics switches contribute to 30% of propulsion system failures [2]; and (v) a dual output that facilitates interfacing to both HVDC and LVDC bus bars. The iDC2 has two outputs, as shown in Figure 2: a main HV and high-current output that processes the power to the HVDC bus and an LV low-current output that provides backup power for the spacecraft's LVDC bus. Note that the LVDC bus is primarily supplied by sources such as solar PV and batteries and is dedicated to the payload. The iDC2 converter includes a three-winding high-frequency (HF) transformer with primary, secondary, and tertiary windings that provide isolation as well as step-up and step-down ratios for the HV and LV outputs. The faults in the iDC2 converter outputs are isolated from the input via the HF transformer, hence providing protection for the TRG and bridge rectifier in case of faults in the HVDC bus, thruster, LVDC bus, or spacecraft power system.

Figure 3 illustrates the region of operation for the propulsion system within the spacecraft, based on the TRG power, speed, and rectified DC voltage. The spacecraft's NEP (Brayton cycle and turbine) provides a speed in the range of 3100 to 4000 RPM for the TRG, while the power may vary from 0 to 3.6 MW due to the varying demand of the electric thruster. As illustrated in Figure 3, the TRG's output power has contributions from its PMR and WFR. The maximum PMR power is 2.5 MW, while the WFR provides the remaining power for the propulsion system, i.e., the region between the two curves in Figure 3. For completeness, Figure 3 shows the power curves for different speeds (0–4000 RPM); however, it is important to note that the propulsion system will only operate in a range of 3100–4000 RPM.

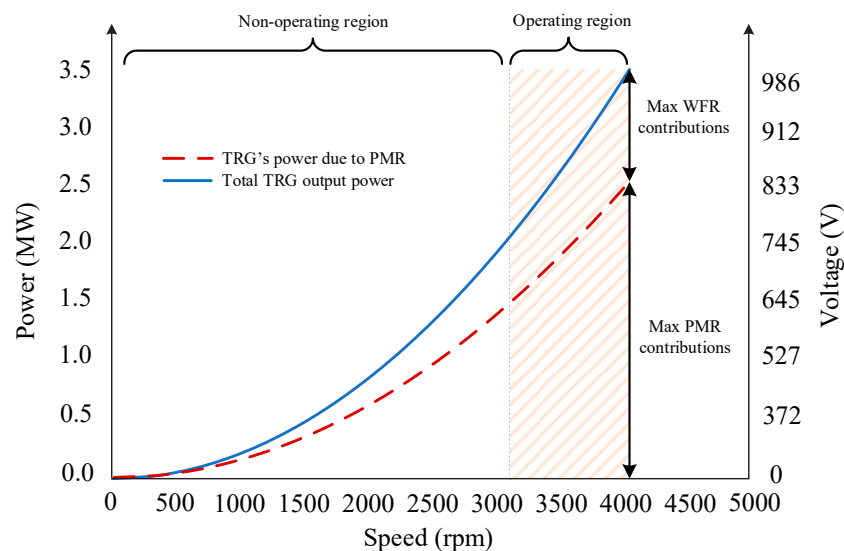


**Figure 3.** Operating regions of propulsion system within the spacecraft.

For the overall speed control of the propulsion system, (i) the TRG's speed is controlled by the NEP; (ii) the sudden changes in the electric thruster demand are controlled by the proposed iDC2 converter; and (iii) the sudden changes that may affect the TRG's frequency in a very short period, such as loss of a phase, may be controlled by designing a speed/frequency controller [14,33–35]; however, this is out of the scope of the paper.

### 3. Design Considerations

#### 3.1. TRG

This section provides a brief overview of the TRG’s parameters and operation. As discussed, the design of the TRG is out of the scope of this paper and has been addressed by the authors in [42–45]. As previously noted, a nine-phase winding configuration results in a 4.2% increase in back-EMF [45], as depicted in the zoomed-in plot in Figure 4a. As the authors in [45] have explained, this is due to an improved winding factor that allows greater flux-linkage and hence back-EMF. In addition, the nine-phase voltage waveshape has a flat top compared to the three-phase sinusoidal shape, which upon rectification, leads to a notably smoother rectified DC voltage in the nine-phase system. Using the TRG design parameter listed in Table 1 [42–45] the 7PMR, WFR, and TRG per phase of the back-EMF for three-phase and nine-phase winding are plotted in Figure 4a. The TRG winding distribution is designed to have an output voltage with a flat top [45], as seen in Figure 4a. Therefore, compared to a sine wave, when rectified, the flat-top waveform results in a lower DC voltage ripple, improving the quality of the passive rectifier output voltage and further reducing the capacitive filtering requirements.

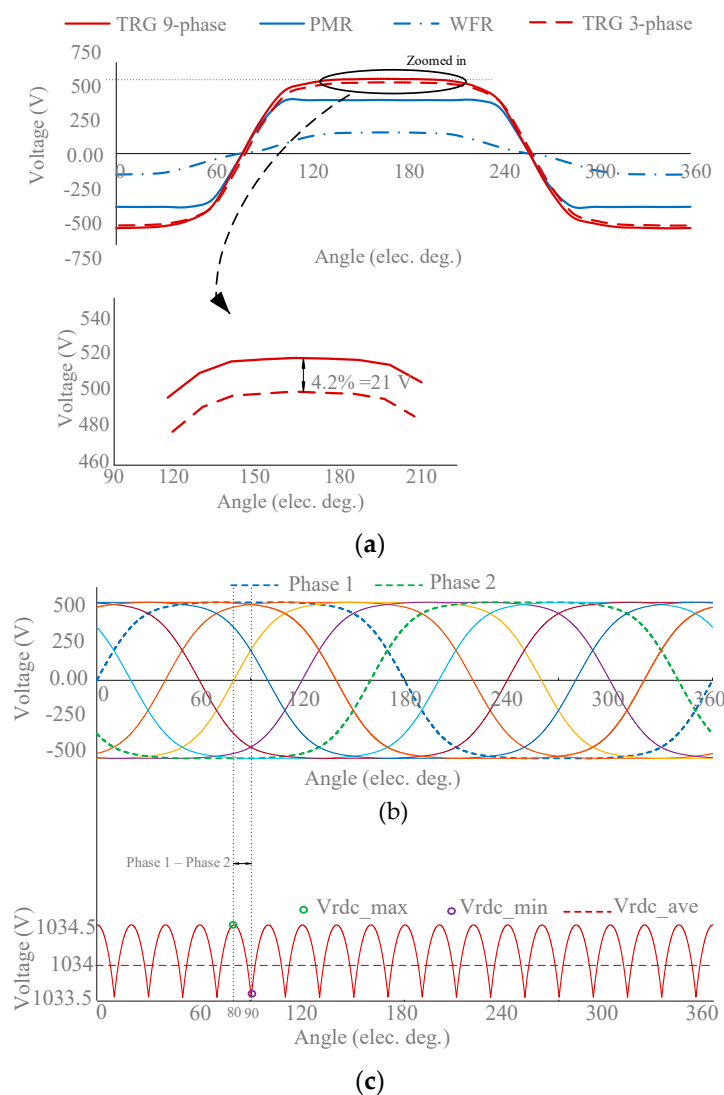


**Figure 4.** (a) Induced voltages of TRG, PMR, and WFR, along with a zoomed-in plot on the TRG nine-phase and three-phase. (b) TRG’s all nine-phase back-EMF (WFR + PMR). (c) The rectified voltage after nine-phase passive rectifier.

**Table 1.** TRG and iDC2 Specifications.

TRG [42–45]	Rated power (MW)	3.6
	Number of poles (p.u.)	10
	Rated speed (rpm)	600
	Nine-phase per-phase RMS back-EMF (V)	579
	Per-phase resistance ( $\Omega$ )	0.7
	Per-phase synchronous inductance (mH)	226.91
	WFR winding resistance ( $\Omega$ )	0.078
iDC2	HVDC bus rated voltage (V)	1000
	LVDC bus rated voltage (V)	200
	Rectified rated DC voltage (V)	1000
	Rated Power (MW)	3.6
	HF transformer turns ratio ( $n_2: n_1$ )	1:1
	HF transformer turns ratio ( $n_3: n_1$ )	0.3:1

The per-phase PMR and WFR back-EMFs, in Figure 4a, as a function of time and based on their harmonic distributions, to represent the trapezoidal waveform, can be expressed as:

$$\begin{aligned}
 e_{pm\_i}(t) &= \hat{e}_{pm\_1i} \sin\left(\omega_e t + \theta_1 - \frac{(i-1)\pi}{n}\right) + \hat{e}_{pm\_2i} \sin\left(2\omega_e t + \theta_2 - \frac{(i-1)\pi}{n}\right) \\
 &\quad + \dots + \hat{e}_{pm\_ki} \sin\left(k\omega_e t + \theta_k - \frac{(i-1)\pi}{n}\right) \\
 e_{wf\_i}(t) &= \hat{e}_{wf\_1i} \sin\left(\omega_e t + \theta_1 - \frac{(i-1)\pi}{n}\right) + \hat{e}_{wf\_2i} \sin\left(2\omega_e t + \theta_2 - \frac{(i-1)\pi}{n}\right) \\
 &\quad + \dots + \hat{e}_{wf\_ki} \sin\left(k\omega_e t + \theta_k - \frac{(i-1)\pi}{n}\right)
 \end{aligned} \quad (2)$$

$$e_{trg\_i}(t) = e_{pm\_i}(t) + e_{wf\_i}(t), \quad i = 1, \dots, n, \quad k = 1, \dots, m, \quad \omega_e = \frac{\omega_m}{p} \quad (3)$$

where  $e_{pm\_i}$  and  $e_{wf\_i}$  are the  $i^{th}$  per-phase back-EMF due to the PMR and WFR, respectively;  $\hat{e}_{pm\_ki}$  and  $\hat{e}_{wf\_ki}$  are the  $i^{th}$  peak per-phase back-EMF due to the PMR and WFR, respectively;  $k$  is the harmonic number;  $e_{trg\_i}$  is the TRG  $i^{th}$  per-phase induced voltage;  $p$  is the number of TRG poles;  $n$  is the number of phases ( $n = 9$ ); and  $m$  is the highest harmonic number in the back-EMF.

In the TRG, the back-EMF generated by the PMR is larger than the WFR back-EMF. This is due to the larger size of the PMR, where the PMR is primarily responsible for the generation of the main power and the WFR's role is in voltage control. As discussed, the nine-phase voltage waveshape has a flat top compared to three-phase sinusoidal shape, which results in reduced rectified voltage ripple. Referring to Figure 4b,c, in a full bridge rectifier, the phase voltage with the highest negative magnitude is subtracted from the phase voltage with the highest positive magnitude at any given time (Phase 1–Phase 2 in Figure 4b, from  $80^\circ$  to  $90^\circ$ ). This subtraction allows us to identify the maximum value for  $v_{rdc}$  at  $80^\circ$  and its minimum at  $90^\circ$ . This can be deduced from Equations (2) and (3) as:

$$\begin{aligned}
 v_{rdc\_max} &= \sum_k \hat{e}_{trg\_k1} \sin(k\omega_e t_1) - \sum_k \hat{e}_{trg\_k2} \sin(k\omega_e t_1), \\
 v_{rdc\_min} &= \sum_k \hat{e}_{trg\_k2} \sin(k\omega_e t_2 - \frac{\pi}{n}) - \sum_k \hat{e}_{trg\_k1} \sin(k\omega_e t_2 - \frac{\pi}{n}),
 \end{aligned} \quad (4)$$

Therefore, the rectified DC voltage ripple is obtained as:

$$\Delta v_{rdcr} = v_{rdc\_max} - v_{rdc\_min} \quad (5)$$

here,  $\hat{e}_{trg\_k1}$  is the TRG's *first* phase-induced voltage and  $\hat{e}_{trg\_k2}$  is the TRG's *second* phase-induced voltage.  $t_1$  and  $t_2$  denote the times when  $v_{rdc}$  reaches its maximum and minimum values, respectively. The phase difference between these two times is  $90^\circ - 80^\circ = 10^\circ$  for a nine-phase full-bridge rectifier, as illustrated in Figure 4c. This figure illustrates a voltage ripple of less than 0.1% compared with 5% for a three-phase rectifier [2]. This leads to a significant reduction in smoothing DC capacitors.

### 3.2. iDC2 Converter

The heat source in the proposed scheme provides a fixed speed for the TRG, whose output is rated at 361 V (phase RMS voltage) and 3.6 MW. At full generation, 90% of the TRG's output power is dedicated to the thruster(s), and the remaining power is reserved for the spacecraft LV power system. From Table 1, and using Equation (1), the average rectified voltage at the output of bridge rectifier is calculated as 1000 V. Given a HVDC bus rated at 1000 V, a transfer ratio of ( $\frac{n_2}{n_1} = 1$ ) is considered from the primary-to-secondary voltage of the HF transformer. For the primary-to-tertiary voltage, a transfer ratio of ( $\frac{n_3}{n_1} = 0.3$ ) is considered, resulting in a rated voltage of 300 V. Of note, the tertiary voltage must be greater than the LVDC spacecraft power system voltage, which is commonly around 200 V [1,2], in order to achieve a positive current flow towards the LVDC power system.

The iDC2 converter includes different conversion stages, shown in Figure 5a. The first conversion is the rectified DC to HF AC power that is formed by the switch  $S_1$  and the magnetizing inductor ( $L_m$ ). The HF AC power is then transferred to two outputs (by a turns ratio of  $\frac{n_2}{n_1}$  and  $\frac{n_3}{n_1}$ ), where in the secondary stage, it is rectified (diode  $D_{hvdc}$ ) and filtered (capacitor  $C_{hvdc}$ ) before connecting to the spacecraft HVDC bus. In the tertiary stage, after rectification and filtering (diode  $D_{lvdc}$  and capacitor  $C_{lvdc}$ ), the current is further increased by a DC-DC step-up stage (switch  $S_2$  and diode  $D_{lvdc\_b}$ ) and filtered (inductor  $L_{lvdc}$ ) before connection to the LVDC bus. Based on the status of switches  $S_1$  and  $S_2$ , the following operational modes are derived:

- Mode 1 (Figure 5b: Switches  $S_1$ : ON,  $S_2$ : ON): Magnetizing inductance  $L_m$  is energized, while the opposite polarity of transformer outputs with respect to the primary reverse-biases diodes  $D_{hvdc}$  and  $D_{lvdc}$  block the output current flow. The capacitors  $C_{hvdc}$  and  $C_{lvdc}$  will discharge to their respective output.
- Mode 2 (Figure 5c: Switches  $S_1$ : OFF,  $S_2$ : ON): Once the switch  $S_1$  turns OFF, the stored energy in  $L_m$  is discharged through the transformer's primary winding to the outputs. Diodes  $D_{hvdc}$  and  $D_{lvdc}$  are forward-biased, transferring the energy to their respective output while charging capacitors  $C_{hvdc}$  and  $C_{lvdc}$ . In this mode, the inductor  $L_{lvdc}$  will be charged, while diode  $D_{lvdc\_b}$  is reverse-biased.
- Mode 3 (Figure 5d: Switches  $S_1$ : OFF,  $S_2$ : OFF): The operation of the converter is similar to in Mode 2; however, in the step-down stage, as switch  $S_2$  turns OFF, the diode  $D_{lvdc\_b}$  is forward-biased, and the inductor  $L_{lvdc}$  will be discharged to the LVDC bus.

To ensure a stable operation, the stored energy in the transformer magnetizing inductor  $L_m$ , when switch  $S_1$  is ON (Figure 5b), must be equal to its released energy when  $S_1$  turns OFF (Figure 5c,d), such that the peak-to-peak  $L_m$  current stays unchanged in steady-state operations. Therefore, considering the opposing polarities of the secondary and tertiary windings of the transformer with respect to the primary winding ((9) as well), the transfer functions from output voltage to input voltage, and the equations for  $d_1$  are presented in (6) and (7).

$$\Delta i_{L_m} = \frac{v_{rdc} d_1}{f_s L_m} = \frac{v_1 (1 - d_1)}{f_s L_m} \quad \text{hence : } \frac{v_{hvdc}(t)}{v_{rdc}(t)} = \frac{d_1}{(1 - d_1)} \frac{n_2}{n_1} \quad (6)$$

$$\text{hence : } d_1 = \frac{v_{hvdc}(t)}{v_{hvdc}(t) + \frac{n_2}{n_1} v_{rdc}(t)} \quad (7)$$

where  $d_1$  and  $f_s$  are the duty cycle and switching frequency of switch  $S_1$ ;  $v_1$  is the voltage across the transformer's primary winding;  $v_{rdc}$  is the average TRG rectified voltage applied to the iDC2 converter input;  $n_1$  and  $n_2$  are the transformer's primary and secondary windings' number of turns, respectively; and  $v_{hvdc}$  is the spacecraft HVDC bus voltage. Note that values represented with "(t)" indicate dynamic values, while those without this notation represent average values.

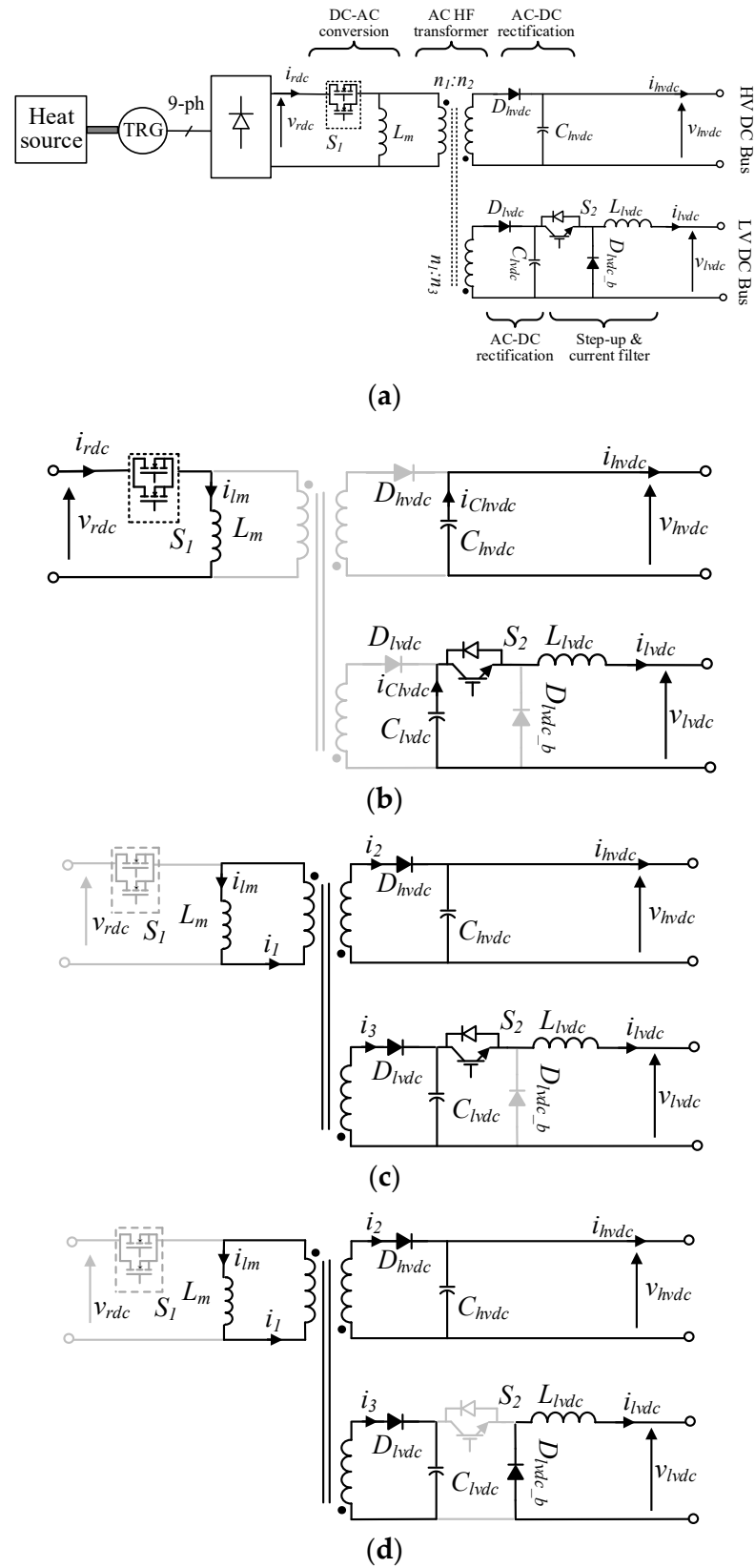


**Figure 5.** iDC2 converter: (a) iDC2 converter conversion stages. (b) mode 1 (Switches  $S_1$ : ON,  $S_2$ : ON). (c) mode 2 (Switches  $S_1$ : OFF,  $S_2$ : ON). (d) mode 3 (Switches  $S_1$ : OFF,  $S_2$ : OFF).

By substituting the averaged currents from (8) into (9), which represents the relationship between transformer's primary, secondary, and tertiary currents ( $i_1, i_2, i_3$ ),  $d_2$  (switch  $S_2$  duty cycle) is determined as (10).

$$i_1 = (1 - d_1)i_{lm} = \frac{(1 - d_1)}{d_1}i_{rdc} \quad i_3 = i_{S2} = d_2i_{lvdc} \quad i_2 = i_{hvdc} \quad (8)$$

$$n_1i_1(t) = n_2i_2(t) + n_3i_3(t) \quad (9)$$

$$\text{hence : } d_2 = \frac{\frac{(1-d_1)}{d_1} i_{rdc} - \frac{n_2}{n_1} i_{hvdc}}{\frac{n_3}{n_1} i_{lvdc}} = \frac{n_2 v_{lvdc}}{n_3 v_{hvdc}} \quad (10)$$

where  $n_3$  is the transformer tertiary windings' number of turns,  $i_{rdc}$  represents the average current at the output of rectifier and the input current of iDC2 converter,  $i_{lm}$  denotes the average current flowing through the magnetizing inductor  $L_m$ ,  $i_{S2}$  is the current that passes through switch  $S_2$ , and  $i_{hvdc}$  and  $i_{lvdc}$  are the average currents injected into the HVDC bus and LVDC bus, respectively, at each desired steady-state operating point.

Given that ( $\frac{n_2}{n_1} = 1$ ,  $\frac{n_3}{n_1} = 0.3$ ), the duty cycles of switches  $S_1$  and  $S_2$  are calculated as  $d_1 = 0.5$  p.u. and  $d_2 = 0.67$  p.u. for the nominal operation using (7) and (10). Of note, these considerations are made solely in the steady-state nominal conditions—when 3.5 MW power is transferring to the HVDC bus and 0.5 MW power is transferring to the LVDC bus. In a closed-loop control, the duty cycles of the switch will vary dynamically to achieve the current/voltage and hence power control.

Given the circuit in Figure 5a and from (8), the magnetizing current is the TRG rectified current ( $i_{rdc}$ ) over switch  $S_1$ 's duty cycle. Assuming that the summation of output powers equals the input power (indicating no power loss), in order to maintain the magnetizing inductor current ripple below a desired level ( $r$  (p.u.) =  $\frac{\Delta i_{lm}}{i_{lm}}$ ), the minimum value for  $L_m$  is given by (11):

$$i_{lm}(t) = \frac{i_{hvdc}v_{hvdc} + i_{lvdc}v_{lvdc}}{v_{rdc} d_1} \quad \text{hence : } L_m > \frac{(v_{rdc} d_1)^2}{f_s r (i_{hvdc}v_{hvdc} + i_{lvdc}v_{lvdc})} \quad (11)$$

where  $v_{lvdc}$  is the spacecraft LVDC bus voltage.

Note that during the design, (11) is calculated for all the possible operating points, and the largest inductance value is selected for the worst-case scenario considering switching frequency and load-range change, such that a margin of 25% is ensured. To compute the inductance of the step-down stage in the tertiary circuit, denoted as  $L_{lvdc}$ , under continuous operation, we need to determine its ripple,  $r$  (p.u.) =  $\frac{\Delta i_{lvdc}}{i_{lvdc}}$ , which is the ratio of the peak-to-peak variation  $\Delta i_{lvdc}$  to the average current,  $i_{lvdc}$ , injected into the LVDC bus during steady-state operation. To ensure a stable operation, the stored energy in the inductor  $L_{lvdc}$  when switch  $S_2$  is ON must be equal to its released energy when  $S_2$  turns OFF, such that the peak-to-peak  $L_{lvdc}$  stays unchanged in steady-state operations. Whether each period of  $S_2$  is on or off can be determined by the equation for  $\Delta i_{lvdc}$ . Here, we consider when switch  $S_2$  is off, so the voltage across the inductor is equal to  $v_{lvdc}$ . As a result, the LVDC inductor is calculated as:

$$\Delta i_{lvdc} = \frac{v_{lvdc}(1 - d_2)}{f_s L_{lvdc}}, \quad \frac{\Delta i_{lvdc}}{i_{lvdc}} = \frac{v_{lvdc}(1 - d_2)}{f_s L_{lvdc} i_{lvdc}} < r, \quad \text{hence : } L_{lvdc} > \frac{v_{lvdc}(1 - d_2)}{f_s r i_{lvdc}} \quad (12)$$

where  $f_s$  is the switching  $S_2$  frequency, which, in this application, we consider to be equal to the switching  $S_1$  frequency.

For the capacitor  $C_{hvdc}$  in the iDC2 converter's secondary output, the HVDC bus voltage ripple,  $r$  (p.u.) =  $\frac{\Delta v_{hvdc}}{v_{hvdc}}$ , appears across it. Given that the capacitor  $C_{hvdc}$  will be

discharged to the output when the diode  $D_{hvdc}$  is reversed-biased, which occurs when the switch  $S_1$  is ON, i.e., during  $d_1 T_s = \frac{d_1}{f_s}$ , the value of capacitor  $C_{hvdc}$  is calculated as:

$$\Delta v_{hvdc} = \frac{\Delta Q_{C_{hvdc}}}{C_{hvdc}} = \frac{d_1 T_s i_{C_{hvdc}}}{C_{hvdc}} = \frac{d_1 T_s i_{hvdc}}{C_{hvdc}} \quad \text{hence : } C_{hvdc} > \frac{d_1 i_{hvdc}}{r f_s v_{hvdc}} \quad (13)$$

where  $\Delta Q_{C_{hvdc}}$  is the charges deposited in the capacitor  $C_{hvdc}$ , and  $i_{C_{hvdc}}$  is the current through capacitor  $C_{hvdc}$ , which is the same as the output current,  $i_{hvdc}$  when  $S_1$  is ON.

On the iDC2's tertiary output, the capacitor  $C_{lvdc}$  will be charged during Mode 3 by  $i_3$  and discharged to the LVDC bus during Mode 1 by  $i_{s2}$ . The average of  $i_3$  is equal to the average value of  $i_{s2}$  considering the discharge time. Therefore, the charges deposited in this capacitor,  $\Delta Q_{C_{lvdc}}$ , considering (8); in turn, the ripple voltage across it is:

$$\Delta Q_{C_{lvdc}} = d_1 T_s i_{s2} = d_1 T_s d_2 i_{lvdc}, \quad \text{hence : } \Delta v_{C_{lvdc}}(t) = \frac{\Delta Q_{C_{lvdc}}}{C_{lvdc}} = \frac{d_1 T_s d_2 i_{lvdc}}{C_{lvdc}} \quad (14)$$

By considering the relationship between the voltages across the transformer, we can derive the relationship between the voltage across the  $C_{lvdc}$  and the HVDC bus voltage. Therefore, ripple  $r$  (p.u.) =  $\frac{\Delta v_{C_{lvdc}}}{v_{C_{lvdc}}}$  across  $C_{lvdc}$ , and finally, the minimum value of  $C_{lvdc}$  based on this desired ripple is:

$$v_{C_{lvdc}} = \frac{n_3}{n_2} v_{hvdc}, \quad \frac{\Delta v_{C_{lvdc}}}{v_{C_{lvdc}}} = \frac{\frac{d_1 T_s d_2 i_{lvdc}}{C_{lvdc}}}{\frac{n_3}{n_1} v_{hvdc}} = \frac{d_1 T_s d_2 i_{lvdc}}{\frac{n_3}{n_1} v_{hvdc} C_{lvdc}} = r, \quad \text{hence : } C_{lvdc} > \frac{d_1 d_2 i_{lvdc}}{\frac{n_3}{n_1} v_{hvdc} r f_s} \quad (15)$$

Here,  $v_{C_{lvdc}}$  is the voltage across  $C_{lvdc}$  in the tertiary stage.

$C_{lvdc}$  is calculated for different operating points, and the highest value is taken as the minimum value of  $C_{lvdc}$  that can satisfy the restrictions. Notably, no circulating current will take place in the circuit due to the presence of capacitor  $C_{lvdc}$ . This capacitor ensures that the circuit achieves equality of  $v_{C_{lvdc}} = \frac{n_3}{n_2} v_{hvdc}$ , as seen in (15), and prevents any current circulation between the outputs.

In light of the recommendation for MW-scale application, as outlined in [35], with a rated current of around 3.6 kA, a thorough investigation is essential for the iDC2 components, particularly the switches and the HF transformer, given the current absence of commercially available components capable of handling such high currents. For switch  $S_1$ , it must withstand a turn-off voltage of 2000 V, necessitating the use of three 2300 V/1800 A IGBTs (e.g., Infineon switches) in parallel to effectively manage the required current. The reference [52] introduces a suitable HF transformer option with specifications of 0.2 kW/1.1 kV, requiring the use of 18 transformers in parallel for the proposed 1 MW/1000 V propulsion system in this paper. Although a high-voltage, high-power transformer specific to the proposed scheme may be designed, such as the one proposed in [53] or space applications, opting for a parallel structure in this scenario offers advantages, as it offers power sharing, increased fault tolerance, and improved reliability. In particular, as the power processed from the heat source is reduced over time [54], a parallel structure of iDC2 aids in utilizing only a portion of it, thus extending the lifespan of the components.

### 3.3. Controllers

In order to develop the HVDC and LVDC controllers for the iDC2 converter that effectively respond to variable load the dynamic models of variables under control, i.e., the inductor currents,  $i_{lm}$ ,  $i_{lvdc}$ , and capacitor voltages,  $v_{hvdc}$ ,  $v_{C_{hvdc}}$ , with respect to the duty cycles of the two switches,  $d_1$  and  $d_2$  are derived. The system state-space model is expressed as:

$$\dot{x} = Ax + Bu, y = Cx + Du, u^T = [\Delta d_1 \Delta d_2 \Delta v_{rdc}], y^T = [\Delta i_{hvdc} \Delta i_{lm} \Delta v_{hvdc} \Delta i_{lvdc}], \dot{x}^T = \left[ \frac{d\Delta i_{Lm}(t)}{dt} \quad \frac{d\Delta v_{hvdc}(t)}{dt} \quad \frac{d\Delta i_{lvdc}(t)}{dt} \right] \quad (16)$$

where  $x$  is the vector of control (state) variables,  $u$  is the vector of inputs,  $y$  is the vector of outputs, and  $A, B, C,$  and  $D$  are the matrices of the linearized system. By rearranging (5) and taking its derivative,  $\frac{\Delta v_{C_{lvdc}}(t)}{dt} = \frac{n_3}{n_2} \frac{dv_{hvdc}(t)}{dt}$ . This equation indicates that changes in  $v_{C_{lvdc}}$  are dependent on the changes in  $v_{hvdc}$ . Therefore, it is unnecessary to incorporate  $v_{C_{lvdc}}$  into the state-space model.

Referring to Figure 5, for Mode 1, the following equations can be derived:

$$\frac{di_{lm}(t)}{dt} = \frac{v_{rdc}(t)}{L_m}, \frac{dv_{hvdc}(t)}{dt} = \frac{n_3 d_2 i_{lvdc}(t) - n_1(1 - d_1) i_{lm}(t)}{n_2 C_{hvdc}}, \frac{di_{lvdc}(t)}{dt} = \frac{\frac{n_3}{n_2} v_{hvdc}(t) - V_{lvdc}}{L_{lvdc}} \quad (17)$$

For Mode 2, the equation for the  $i_{lvdc}$  from (17) is held, but the other equations change to:

$$\frac{di_{lm}(t)}{dt} = -\frac{n_1}{n_2} \frac{v_{hvdc}(t)}{L_m}, \frac{dv_{hvdc}(t)}{dt} = \frac{-(1 - d_2(t)) \frac{n_3}{n_2} i_{lvdc}(t) + d_1(t) \frac{n_1}{n_2} i_{lm}(t)}{C_{hvdc} + C_{lvdc} \left(\frac{n_3}{n_2}\right)^2} \quad (18)$$

For Mode 3, the equation for  $i_{lm}$  from (18) is held, but the  $i_{lvdc}, v_{hvdc}$  equations change to:

$$\frac{di_{lvdc}(t)}{dt} = \frac{-V_{lvdc}}{L_{lvdc}}, \frac{dv_{hvdc}(t)}{dt} = \frac{d_2(t) \frac{n_3}{n_2} i_{lvdc}(t) + d_1(t) \frac{n_1}{n_2} i_{lm}(t)}{C_{hvdc} + C_{lvdc} \left(\frac{n_3}{n_2}\right)^2} \quad (19)$$

By taking the average of variables' derivatives over one switching period, as represented in Figure 5b, the linearized average models of the variables are obtained as follows:

$$\begin{aligned} \frac{di_{lm}(t)}{dt} &= d_1(t) \frac{v_{rdc}(t)}{L_m} - (1 - d_1(t)) \left( \frac{n_1}{n_2} \frac{v_{hvdc}(t)}{L_m} \right), \frac{di_{lvdc}(t)}{dt} = d_2(t) \frac{v_{hvdc}(t)}{L_{lvdc}} \frac{n_3}{n_2} - \frac{V_{lvdc}}{L_{lvdc}}, \\ \frac{dv_{hvdc}(t)}{dt} &= \frac{\frac{n_3}{n_2} d_1(t) d_2(t) i_{lvdc}(t) - \frac{n_1}{n_2} d_1(t) (1 - d_1(t)) i_{lm}(t)}{C_{hvdc}} \\ &+ \frac{\frac{n_3}{n_2} d_1(t) (1 - d_2(t)) i_{lvdc}(t) + \frac{n_1}{n_2} d_1(t) (1 - d_1(t)) i_{lm}(t)}{C_{hvdc} + C_{lvdc} \left(\frac{n_3}{n_2}\right)^2} \end{aligned} \quad (20)$$

Furthermore, by rearranging (7) and (9), the averaged model for  $i_{hvdc}$  is:

$$i_{hvdc}(t) = \frac{n_1}{n_2} (1 - d_1(t)) i_{lm}(t) - \frac{n_3}{n_2} d_2(t) i_{lvdc}(t) \quad (21)$$

Using the Jacobian approach [54], the system is linearized, for which the state-space model matrices based on (16) are as below.  $A_{12}$  to  $D_{12}$  denote the non-zero values introduced in matrices  $A, B, C,$  and  $D$ .

$$\begin{aligned}
 A &= \begin{bmatrix} 0 & A_{12} & 0 \\ A_{21} & 0 & A_{23} \\ 0 & A_{32} & 0 \end{bmatrix}, \quad B = \begin{bmatrix} B_{11} & 0 & B_{13} \\ B_{21} & 0 & B_{23} \\ 0 & B_{32} & 0 \end{bmatrix}, \quad C = \begin{bmatrix} C_{11} & 0 & C_{13} \\ 1 & 0 & 0 \\ 0 & 1 & 0 \\ 0 & 0 & 1 \end{bmatrix}, \quad D = \begin{bmatrix} D_{11} & D_{12} & 0 \\ 0 & 0 & 0 \\ 0 & 0 & 0 \\ 0 & 0 & 0 \end{bmatrix} \\
 A_{12} &= \frac{n_1}{n_2} \frac{1}{L_m} (d_1 - 1), \quad A_{21} = \frac{\frac{n_1}{n_2} (d_1 - d_1^2)}{C_{hvdc} + C_{lvdc} \left(\frac{n_3}{n_2}\right)^2} - \frac{\frac{n_1}{n_2} (d_1 - d_1^2)}{C_{hvdc}}, \\
 A_{23} &= \frac{\frac{n_3}{n_2} (d_1 - d_1 d_2)}{C_{hvdc} + C_{lvdc} \left(\frac{n_3}{n_2}\right)^2} - \frac{\frac{n_3}{n_2} d_1 d_2}{C_{hvdc}}, \quad A_{32} = d_2 \frac{n_3}{n_2} \frac{1}{L_{lvdc}}, \quad B_{11} = \frac{v_{rdc}}{L_m} + \frac{n_1}{n_2} \frac{v_{lvdc}}{L_m} \\
 B_{13} &= \frac{d_1}{L_m}, \quad B_{21} = \frac{\frac{n_3}{n_2} (1 - d_2) i_{lvdc} - 2 \frac{n_1}{n_2} d_1 i_{lm}}{C_{hvdc} + C_{lvdc} \left(\frac{n_3}{n_2}\right)^2} + \frac{\frac{n_3}{n_2} d_2 i_{lvdc} - 2 \frac{n_1}{n_2} d_1 i_{lm}}{C_{hvdc}}, \quad B_{32} = \frac{v_{lvdc}}{L_{lvdc}} \frac{n_3}{n_2} \\
 B_{23} &= \frac{-\frac{n_3}{n_2} d_1 i_{lvdc}}{C_{hvdc} + C_{lvdc} \left(\frac{n_3}{n_2}\right)^2} + \frac{\frac{n_3}{n_2} d_1 i_{lvdc}}{C_{hvdc}}, \quad C_{11} = \frac{n_1}{n_2} (1 - d_1), \quad C_{13} = -\frac{n_3}{n_2} d_2 \\
 D_{11} &= -\frac{n_1}{n_2} i_{lm}, \quad D_{12} = -\frac{n_3}{n_2} i_{lvdc}
 \end{aligned} \tag{22}$$

Figure 6 shows a simplified model of the iDC2 controllers using the obtained averaged and linearized steady-state model. In order to control HVDC current, a dual-loop controller is utilized, whereas a single-loop control is implemented for the other two. The purpose of employing a dual-loop controller is to detect changes in the current,  $i_{lm}$ , ahead of its utilization at the HVDC bus [55–57]. This approach allows the HVDC current controller to respond faster and operate more smoothly within the closed-loop system. In the specific context of this application, designing a controller based on a single operating point, as confirmed by the simulation results in Section 4, can offer sufficient robustness. This is because there are constraints on how quickly the power output of reactors can be altered. Consequently, the input power for PMAD cannot vary widely within a short time span, leading to other operating points typically remaining close to the selected one for a PI controller. Other advanced control approaches, such as the use of artificial intelligence base controls [58], would improve the dynamic performance of the proposed controllers and the iDC2 converter; however, these are out of the scope of this paper.

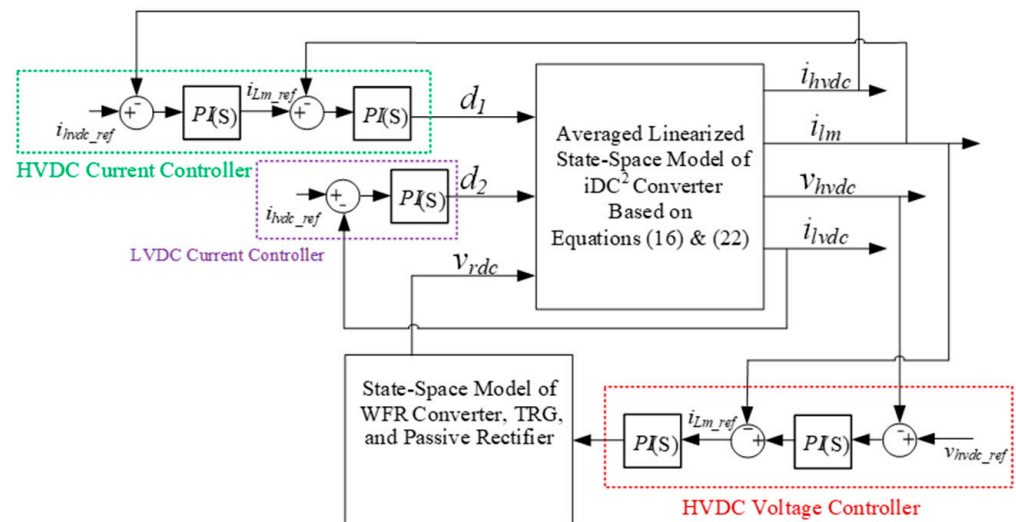


Figure 6. iDC2 converter simplified controllers.

#### 4. Simulation

To validate the proposed scheme and verify the effectiveness and accuracy of the proposed controllers, a simulation platform of the entire system, depicted in Figure 2, was developed. The simulation incorporates the TRG specifications outlined in Table 1 and employs the component values for the iDC2 converter specified in Table 2. The switching frequency is set to 3 kHz, and current/voltage ripple levels of below 5% are targeted.

Figure 7 shows the simulation results when a sudden increase in thruster power occurs at 5 s, followed by a sudden decrease in 10 s.

**Table 2.** iDC2 Components.

No. of primary turns ( $N_1$ )	1000
No. of secondary turns ( $N_2$ )	1000
No. of tertiary turns ( $N_3$ )	300
Primary magnetizing inductance ( $L_m$ )	598 mH
Step-down stage inductance ( $L_{Ivdc}$ )	1.78 mH
Tertiary capacitance ( $C_{Ivdc}$ )	8230 $\mu$ F
Secondary capacitance ( $C_{hvdc}$ )	8772 $\mu$ F

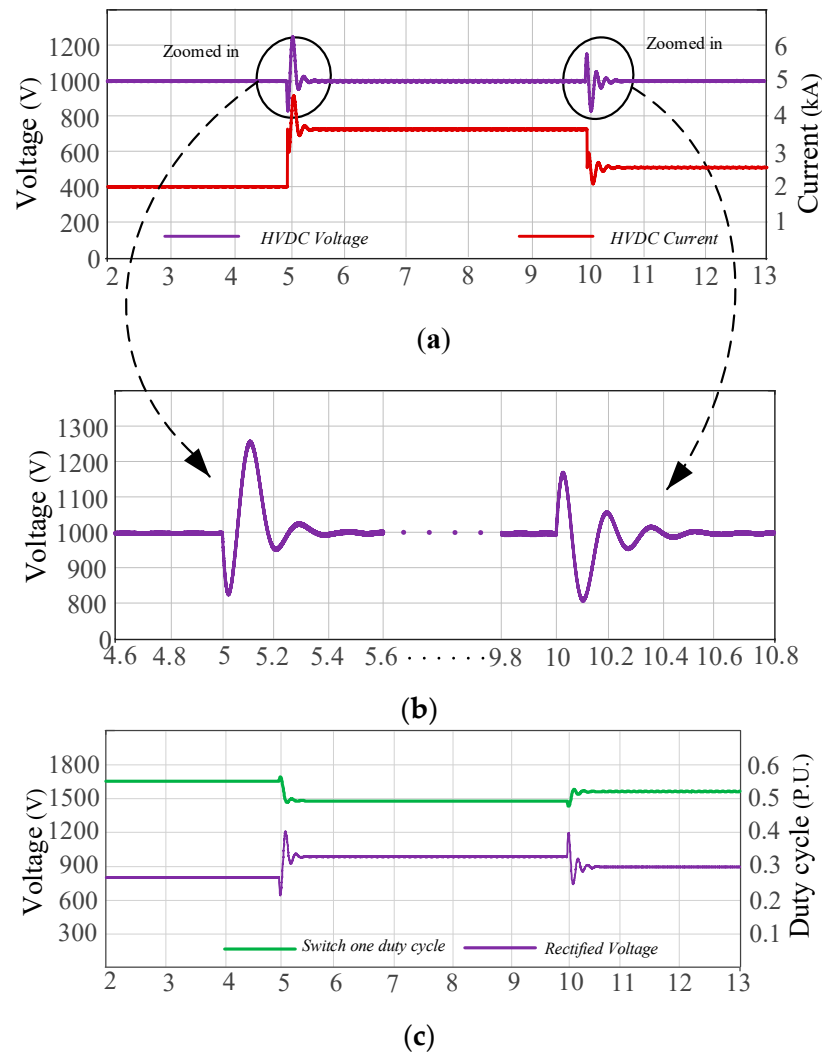


**Figure 7.** Simulation results for HVDC controllers: (a) HVDC input voltage and current. (b) Zoomed-in plots of HVDC voltage. (c) Switch  $S_1$  duty cycle ( $d_1$ ) and rectified voltage after passive rectifier.

As seen from Figure 7a, the HVDC output current ( $i_{hvdc}$ ) varies with the thruster power demand, while the HVDC voltage controller maintains the HVDC voltage around its nominal value (1000 V). The transients are shown in the zoomed-in plot of Figure 7b, which demonstrates that it takes less than 0.5 s for the controller to settle down the HVDC voltage and current; this is much faster than the requirements of spacecraft controls. Figure 7c shows that the controller adjusts the duty cycle of switch  $S_1$  ( $d_1$ ), depending on the rectified voltage at the output of passive rectifier ( $v_{rdc}$ ), which can be varied based on the WFR

segment of the TRG. When the power demand increases at 5 s, the input voltage to the iDC2 converter ( $v_{rdc}$ ) should go up, because  $d_1$  decreases in order to provide a higher current for HVDC bus. In other words,  $d_1$  and  $v_{rdc}$  serve as two inputs, jointly controlling the HVDC bus's current and voltage. Similarly, as the thruster power demand reduces at 10 s,  $d_1$  increases and  $v_{rdc}$  decreases to reduce the HVDC current and keep the HVDC voltage at 1000 V. Figure 8 shows the results for the LVDC bus, while the thruster power demand varies in the same manner as in Figure 7. However, with LVDC bus power, the spacecraft power demand reduced from 200 kW to 150 kW at 5 s and then reduced to 100 kW at 10 s.

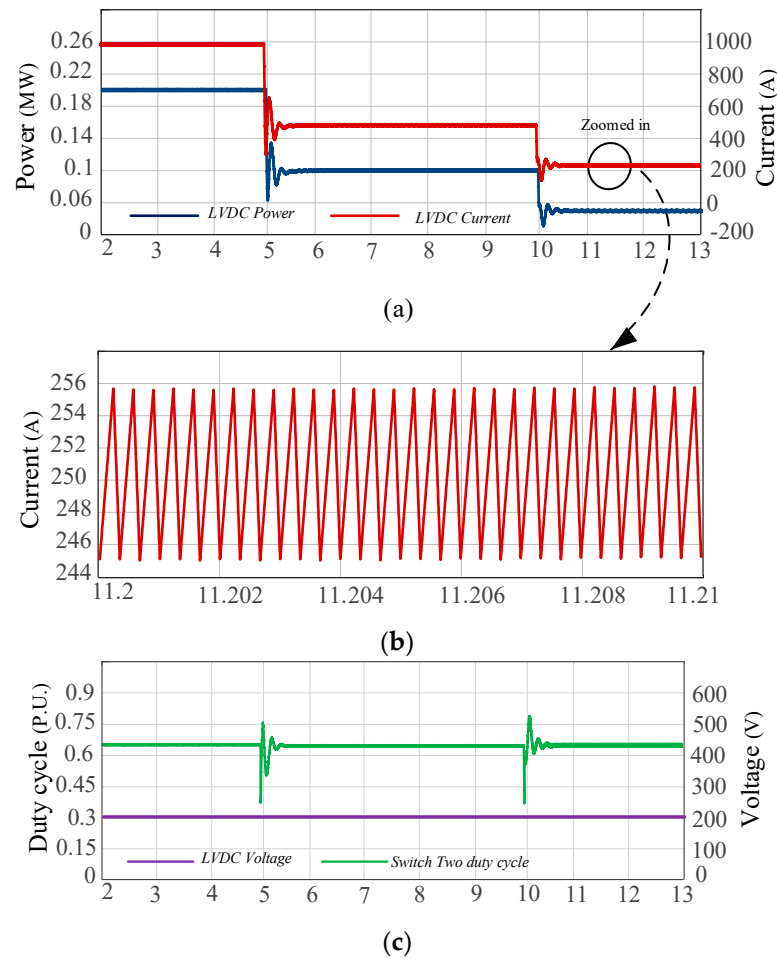


**Figure 8.** Simulation results for LVDC controller. (a) LVDC current and power. (b) Zoomed-in LVDC current, showing ripple. (c) LVDC voltage and switch  $S_2$  duty cycle ( $d_2$ ).

As shown in Figure 8a, the LVDC controller adjusts the current as the power demand varies, while the LVDC bus voltage is maintained (Figure 8c). Notably, the LVDC bus is fixed by the spacecraft's low-voltage battery system and its associated DC-DC converter, as schematically shown in Figure 2. The duty cycle of switch  $S_2$  ( $d_2$ ) shows that it stays close to its nominal value (0.66 p.u.) as the LVDC bus power changes. This is due to constant  $v_{lvdc}$  and  $v_{hvdc}$  at all times and based on (10). The zoomed-in plot of the LVDC current in Figure 8b shows a ripple of 2.4%, which is below the target value of 5%, hence confirming the suitability of the design and component selection.

Table 3 lists the predicted results from the analytical modeling, which are the averaged values obtained from the equations in Section 3.2. The comparison of results in Table 3 and those of Figures 7 and 8, which display the results of the closed-loop control system, serves to validate the suitability of the proposed topology for spacecraft EP systems and verify the analytical models and functionality of the proposed controllers.

**Table 3.** Results from analytical model.

Time	2–5 s	5–10 s	10–13 s
HVDC power	2 MW	3.5 MW	2.5 MW
LVDC power	0.2 MW	0.1 MW	0.05 MW
HVDC current	2000 A	3500 A	2500 A
LVDC current	1000 A	500 A	250 A
HVDC voltage	1000 V	1000 V	1000 V
Rectified voltage	800 V	1000 V	900 V
Switch $s_1$ duty cycle	0.55556	0.5	0.526
Switch $s_2$ duty cycle	0.66667	0.66667	0.66667
HVDC power	2 MW	3.5 MW	2.5 MW
LVDC power	0.2 MW	0.1 MW	0.05 MW

## 5. Experimental Results

To evaluate the analytical design, a small-scale laboratory prototype experimental setup was developed as illustrated in Figure 9. The setup comprised (i) an induction motor that acts as a fixed-speed prime mover for the TRG, (ii) a scaled-down nine-phase TRG prototype built in-house from the previous work of the authors [35], (iii) a nine-phase passive rectifier that rectifies the output of the TRG, (iv) an iDC2 converter, (v) an Arduino programmed with the functionality of the proposed controllers tailored to support this scaled-down prototype to control the LVDC and HVDC outputs, and (vi) a DC power supply that emulates the spacecraft fixed LVDC bus. Designed for laboratory use, the prototype supports an iDC2 HVDC output rated at 140 V and a 20 V LVDC output, capable of sustaining a peak current of 25 A at 130 V.

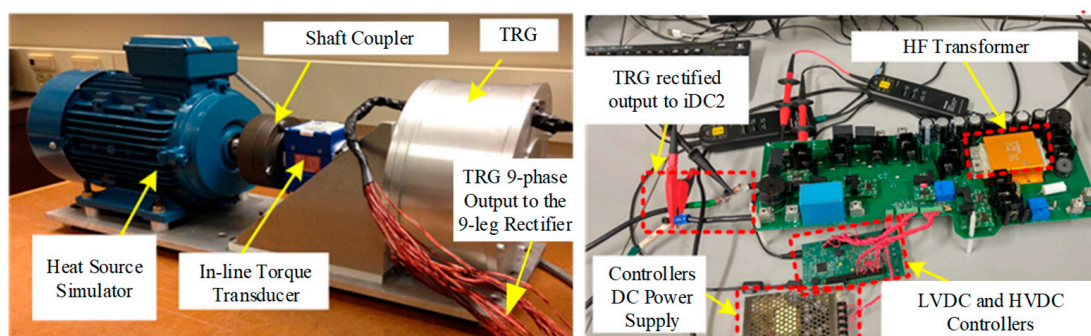
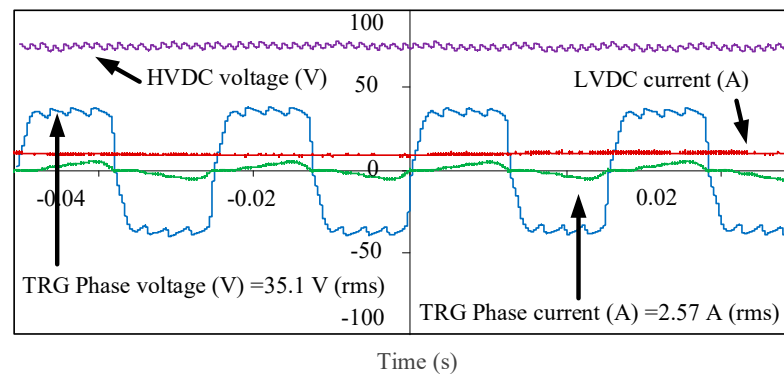
**Figure 9.** Experimental setup.

Table 4 presents the prototype specifications, consisting of the rated value of the setup alongside a particular operating point, leading to the results displayed in Figure 11.

**Table 4.** Prototype Specifications.

Setup Information	IM max. speed	3000 RPM
	IM rated power	2 kW
	TRG rated phase back-EMF	75 V RMS
	TRG rated power	2 kW
	TRG number of phases	9 (concentric winding)
	iDC2 rated voltage	100 V DC
	iDC2 rated current	30 A
Experimental Results (Shown in Figure 11, based on the O.P. shown in Figure 10)	IDC2 HVDC output voltage	75 V @ tested O.P.
	IDC2 HVDC output current	10 A @ tested O.P.
	IDC2 LVDC output current	10 A @ tested O.P.
	IDC2 LVDC output voltage	20 V fixed



**Figure 10.** Comparison of experimental and analytical results for different iDC2 HVDC output current and voltage, and LVDC current.

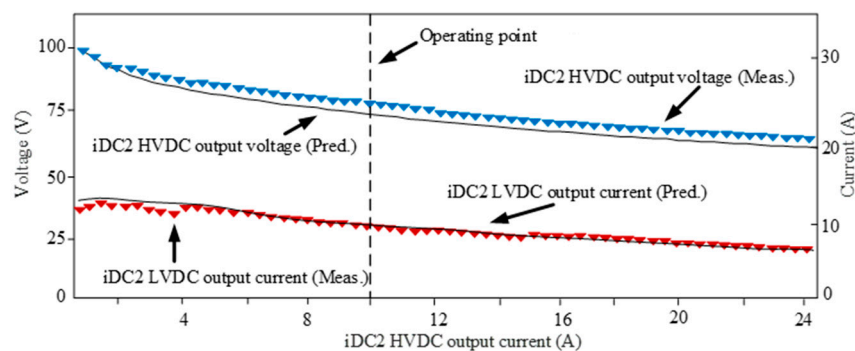


**Figure 11.** Experimental results for iDC2 outputs, and TRG phase values.

Under these conditions, the load on the iDC2 HVDC output is fixed at 750 W. It is observed that the HVDC controllers effectively sustain the output voltage at a targeted 75 V during load transitions. The fluctuations in HVDC voltage are the result of fluctuations in the TRG's voltage at the peak, which is a contribution of the nine-phase winding, showing the moments the commutation changes between the diodes in the passive rectifier. The HVDC voltage and LVDC current show ripples of less than 0.05 p.u., demonstrating that the components of iDC2 are designed effectively for this laboratory prototype. This stability is attributed to the rotor's consistent position, ensuring the back-EMF remains constant. The TRG phase current and phase voltage (total of the PMR and WFR at each phase) also denote the power generated by the TRG, which is in total  $p_{TRG} = 9 \times v_{TRG\_phase\_rms} \times i_{TRG\_phase\_rms} \approx 950 \text{ W}$  (as the generator winding is designed for nine phases) [46], equating to the sum of output powers, as indicated in Table 4. This equality confirms the functionality of the nine-phase operation. The data demonstrate that the controllers are proficient in maintaining their designated outputs at the considered operating point (O.P.) for this test.

Figure 10 displays the actual measurements alongside the predicted results for the iDC2 outputs under various loads (different O.P.). This graph depicts the load variation through the HVDC output current, ranging from no load to a maximum of 25 A DC. During this testing, we aim to keep the power from the TRG under 2 kW as introduced as the rated power in Table 4. As observed, when the HVDC current increases, the HVDC voltage decreases, while the LVDC current decreases accordingly to avoid surpassing the power limitations of the system. This figure aims to showcase the system's capability under various HVDC loads, demonstrating that as the HVDC load increases, the system can allocate less power to the LVDC load. Note that for this test, iDC2 does not attempt to maintain HVDC voltages at a constant value. Instead, it adjusts them to the desired value to remain within the system's capability. The matching outcomes between the simulations and

the actual measurements in Figure 10 also provide confirmation that the design, models, and proposed controllers are functioning correctly.

## 6. Conclusions

The proposed electrical power-conversion system outlined in this study offers advantages for power management and distribution (PMAD) in large spacecraft. Through the integration of a two-rotor generator (TRG) featuring a permanent magnet rotor (PMR) and a wound field rotor (WFR), along with an isolated dual output DC-DC converter (iDC2), this configuration enables control over three critical outputs: (I) the voltage applied to the electric thruster, (II) the power delivered to the electric thruster, and (III) the backup power supplied to the spacecraft's power system. The iDC2 converter's robust design includes fault isolation features via a high-frequency transformer, ensuring system protection against faults in the HVDC bus, thruster, LVDC bus, or spacecraft power system. Moreover, the overall control provided by iDC2 permits the utilization of a passive rectifier after the TRG, significantly enhancing the reliability of the entire system. Validations through simulation studies confirm the effectiveness of the proposed control strategies in responding to variable load conditions. The dual-loop controller for HVDC outputs ensures smooth operation and rapid adjustment to power demand fluctuations in experimental laboratory works. Results demonstrate the system's ability to manage sudden changes in thruster power demand while maintaining HVDC bus voltages within specified limits. Furthermore, the design and component selection yield ripple levels below target values, affirming the suitability and reliability of the proposed scheme for in-space electric propulsion applications. The unidirectional nature of iDC2 facilitates precise power allocation to each output. However, future research could explore implementing bidirectional functionality for the secondary and tertiary sides of the transformer. This enhancement would enable power exchange between components, especially during scenarios where the TRG encounters sudden changes or during braking mode, allowing excess power to be redirected to the spacecraft's power system as needed.

**Author Contributions:** Conceptualization, O.B.; Methodology, O.B.; Software, G.S.; Validation, O.B.; Formal analysis, G.S. and O.B.; Investigation, G.S. and O.B.; Resources, O.B.; Data curation, O.B.; Writing—original draft, G.S. and O.B.; Writing—review & editing, O.B.; Supervision, O.B.; Project administration, O.B.; Funding acquisition, O.B. All authors have read and agreed to the published version of the manuscript.

**Funding:** This work was funded in part by NASA—Award Number: FAR0029766.

**Data Availability Statement:** Data is contained within the manuscript.

**Conflicts of Interest:** The authors declare no conflict of interest.

## References

1. Beik, O.; Patel, M.R.; Talebzadeh, S. Large Spacecraft Electric Propulsion Using Multiphase Generator. In Proceedings of the 2023 IEEE Aerospace Conference, Big Sky, MT, USA, 4–11 March 2023; pp. 1–8.
2. Patel, M.R.; Beik, O. *Spacecraft Power Systems*; CRC Press: Boca Raton, FL, USA, 2023.
3. Krejci, D.; Lozano, P. Space Propulsion Technology for Small Spacecraft. *Proc. IEEE* **2018**, *106*, 362–378. [CrossRef]
4. Djamal, D.; Mohamed, K.; Aslan, A.R. RESISTOJET Propulsion System for Small Satellite. In Proceedings of the 9th International Conference on Recent Advances in Space Technologies (RAST), Istanbul, Turkey, 11–14 June 2019.
5. Jovel, D.R.; Walker, M.L.R.; Herman, D. Review of High-Power Electrostatic and Electrothermal Electric Propulsion. *J. Propuls. Power* **2022**, *38*, 1051–1081. [CrossRef]
6. NASA—Ion Propulsion. Available online: <https://www.nasa.gov/centers/glenn/about/fs21grc.html> (accessed on 10 August 2023).
7. Psyche's Hall Thruster. Available online: <https://www.jpl.nasa.gov/images/pia24030-psyches-hall-thruster> (accessed on 10 August 2023).
8. Polzin, K.; Martin, A.; Little, J.; Promislow, C.; Jorns, B.; Woods, J. State-of-the-Art and Advancement Paths for Inductive Pulsed Plasma Thrusters. *Aerospace* **2020**, *7*, 105. [CrossRef]
9. Baranov, O.O.; Cvelbar, U.; Bazaka, K. Concept of a Magnetically Enhanced Vacuum Arc Thruster with Controlled Distribution of Ion Flux. *IEEE Trans. Plasma Sci.* **2018**, *46*, 304–310. [CrossRef]

10. Gonzalez-Llorente, J.; Lidtke, A.A.; Hatanaka, K.; Kawauchi, R.; Okuyama, K.-I. Solar Module Integrated Converters as Power Generator in Small Spacecrafts: Design and Verification Approach. *Aerospace* **2019**, *6*, 61. [CrossRef]
11. Matthes, C.S.R.; Woerner, D.F.; Hendricks, T.J.; Fleurial, J.-P.; Oxnevad, K.I.; Barklay, C.D.; Zakrajsek, J.F. Next-generation radioisotope thermoelectric generator study. In Proceedings of the 2018 IEEE Aerospace Conference, Big Sky, MT, USA, 3–10 March 2018; pp. 1–9.
12. DART: Double Asteroid Redirection Test. 2022. Available online: <https://dart.jhuapl.edu/Mission/> (accessed on 10 August 2023).
13. Voyager 1 & 2. Available online: <https://rps.nasa.gov/missions/12/voyager-1-2/> (accessed on 10 August 2023).
14. Braun, B.; Myers, R. *Space Nuclear Propulsion for Human Mars Exploration*; The National Academies of Sciences: Washington, DC, USA, 2021.
15. Peakman, A.; Lindley, B. A review of nuclear electric fission space reactor technologies for achieving high-power output and operating with HALEU fuel. *Prog. Nucl. Energy* **2023**, *163*, 104815. [CrossRef]
16. Meyer, M.L.; Hartwig, J.W.; Sutherlin, S.G.; Colozza, A.J. Recent concept study for cryogenic fluid management to support opposition class crewed missions to Mars. *Cryogenics* **2023**, *129*, 103622. [CrossRef]
17. Borowski, S.K.; McCurdy, D.R.; Packard, T.W. Nuclear Thermal Propulsion (NTP): A proven growth technology for human NEO/Mars exploration missions. In Proceedings of the 2012 IEEE Aerospace Conference, Big Sky, MT, USA, 3–10 March 2012; pp. 1–20.
18. Nikitaeva, D.; Thomas, L.D. Propulsion Alternatives for Mars Transportation Architectures. *J. Spacecr. Rocket.* **2023**, *60*, 520–532. [CrossRef]
19. Nikitaev, D.; Thomas, L.D. Impacts of In Situ Alternative Propellant on Nuclear Thermal Propulsion Mars Vehicle Architectures. Available online: <https://www1.grc.nasa.gov/space/sep/gridded-ion-thrusters-next-c/> (accessed on 10 August 2023).
20. Shen, D.; Yue, Y.; Wang, X. Manned Mars Mission Analysis Using Mission Architecture Matrix Method. *Aerospace* **2022**, *9*, 604. [CrossRef]
21. Machemer, W.S.; Duchek, M.E.; Nikitaev, D. Considerations for Radiator Design in Multi-Megawatt Nuclear Electric Propulsion Applications. In Proceedings of the AIAA SCITECH Forum 2023, National Harbor, MD, USA, 23–27 January 2023.
22. Oleson, S.R.; Burke, L.M.; Ma son, L.S.; Turnbull, E.R.; Mccarty, S.; Colozza, A.J.; Fittje, J.E.; Yim, J.T.; Smith, M.; Packard, T.W.; et al. Compass Final Report: Nuclear Electric Propulsion (NEP)–Chemical Vehicle 1.2. No. CD-2020-181. 2021. Available online: [https://ntrs.nasa.gov/api/citations/20210017131/downloads/TM-20210017131\\_errata.pdf](https://ntrs.nasa.gov/api/citations/20210017131/downloads/TM-20210017131_errata.pdf) (accessed on 28 March 2024).
23. Kokan, T.S.; Horton, J.F.; Joyner, C.R.; Levack, D.J.; Morris, D.E.; Muzek, B.J.; Noble, R.W.; Reynolds, C.B. Nuclear Electric Propulsion/Chemical Propulsion Hybrid Human Mars Exploration Campaign: From Start to Steady-State. In Proceedings of the ASCEND 2021, Las Vegas, NV, USA, 15–17 November 2021; p. 4013.
24. Duchek, M.; Clark, M.; Pensado, A.; Harnack, C.; Machemer, W.; Grella, E.; Qu, M. Hybrid NEP-Chemical Vehicle and Propulsion Technology Study for Crewed Mars Missions. In Proceedings of the 68th JANNAF Propulsion Meeting 2021, Virtual, 7–17 June 2021.
25. *Independent Assessment of the Technical Maturity of Nuclear Electric Propulsion (NEP) and Nuclear Thermal Propulsion (NTP) Systems*; NASA Engineering & Safety Center: Hampton, VA, USA, 2020.
26. Polzin, K.A.; Martin, A.K.; Curran, A.; Myers, R.; Rodriguez, M. Strategy for Developing Technologies for Mega-watt-class Nuclear Electric Propulsion Systems. In Proceedings of the International Electric Propulsion Conference, Boston, MA, USA, 19–23 June 2022.
27. Martin, A.K.; Polzin, K.A.; Curran, F.M.; Myers, R.M.; Rodriguez, M.A. A Technology Maturation Plan for the Development of Nuclear Electric Propulsion. In Proceedings of the Joint Army-Navy-NASA-Air Force (JANNAF) Meeting, Huntsville, AL, USA, 5–9 December 2022.
28. Harnack, C.; Machemer, W.; Duchek, M.; Grella, E.; Nikitaev, D.; Smith, C. Brayton Cycle Power Conversion Model for MW-Class Nuclear Electric Propulsion Mars Missions. In Proceedings of the Nuclear and Emerging Technologies for Space (NETS-2022), Cleveland, OH, USA, 8–12 May 2022.
29. Nikitaev, D.; Smith, C.; Duchek, M.; Harnack, C.; Machemer, W.; Grella, E. Nuclear Electric Propulsion Modular Power Conversion Model. In Proceedings of the Nuclear and Emerging Technologies for Space (NETS-2022), Cleveland, OH, USA, 8–12 May 2022.
30. Machemer, W.; Duchek, M.; Harnack, C.; Grella, E.; Nikitaev, D.; Smith, C. Mass Modeling of NEP Power Conversion Concepts for Human Mars Exploration. In Proceedings of the Nuclear and Emerging Technologies for Space (NETS-2022), Cleveland, OH, USA, 8–12 May 2022.
31. Nikitaev, D.; Duchek, M.E.; Harnack, C.; Machemer, W.; Rao, D. Heat Pipe Heat Exchanger for Nuclear Electric Propulsion Power Conversion System. In Proceedings of the AIAA ASCEND 2022, Las Vegas, NV, USA, 24–26 October 2022.
32. Dyson, R.; Rao, D.; Duchek, M.; Harnack, C.; Scheidegger, R.; Mason, L.; Juhasz, A.; Rodriguez, L.; Leibach, R.; Geng, S.; et al. Nuclear Electric Propulsion Brayton Power Conversion Working Fluid Considerations. In Proceedings of the Nuclear and Emerging Technologies for Space (NETS-2022), Cleveland, OH, USA, 8–12 May 2022.
33. Li, Z.; Yang, X.; Wang, J.; Zhang, Z. Off-design performance and control characteristics of space reactor closed Brayton cycle system. *Ann. Nucl. Energy* **2019**, *128*, 318–329. [CrossRef]
34. Koroteev, A.S.; Oshev, Y.A.; Popov, S.A.; Karevsky, A.V.; Solodukhin, A.Y.; Zakharenkov, L.E.; Seminkin, A.V. Nuclear power propulsion system for spacecraft. *Therm. Eng.* **2015**, *62*, 971–980. [CrossRef]

35. Nuclear Electric Propulsion. Available online: <https://nap.nationalacademies.org/read/25977/chapter/5> (accessed on 10 March 2024).
36. Harnack, C.; Machemer, W.; Nikitaeva, D.; Duchek, M. Component-level Performance and Mass Sensitivity Analysis of NEP MW-class Power System. In Proceedings of the AIAA ASCEND 2022, Las Vegas, NV, USA, 24–26 October 2022.
37. Duchek, M.; Machemer, W.; Harnack, C.; Clark, M.A.; Pensado, A.R.; Palomares, K.B.; Polzin, K.A.; Martin, A.; Curran, F.; Myers, R.; et al. Key Performance Parameters for MW-Class NEP Elements and their Interfaces. In Proceedings of the AIAA ASCEND 2022, Las Vegas, NV, USA, 24–26 October 2022.
38. Bidirectional Dual Active Bridge Power Converter for Spacecraft Power Systems. Available online: <https://techport.nasa.gov/view/90266> (accessed on 28 March 2024).
39. *State-of-the-Art of Small Spacecraft Technology*; NASA: Washington, DC, USA, 2024.
40. Polzin, K. *Technology Development for In-Space Nuclear Electric Propulsion*; Marshall Space Flight Center: Huntsville, AL, USA, 2021.
41. Soeder, R.S.J. *Spacecraft Bus Voltage Selection*; NASA Glenn Research Center: Cleveland, OH, USA, 2015.
42. Al-Adsani, A.S.; Jarushi, A.M.; Beik, O. ICE/HPM generator range extender for a series hybrid EV powertrain. *IET Electr. Syst. Transp.* **2020**, *10*, 96–104. [[CrossRef](#)]
43. Al-Adsani, A.S.; Beik, O. *Multiphase Hybrid Electric Machines: Application for Electrified Powertrains*; Springer International: Cham, Switzerland, 2021.
44. Beik, O.; Schofield, N. High-Voltage Hybrid Generator and Conversion System for Wind Turbine Applications. *IEEE Trans. Ind. Electron.* **2017**, *65*, 3220–3229. [[CrossRef](#)]
45. Beik, O.; Al-Adsani, A.S. A Wind Turbine Generator Design and Optimization for DC Collector Grids. *IEEE J. Emerg. Sel. Top. Power Electron.* **2021**, *10*, 484–493. [[CrossRef](#)]
46. Balasubramanian, S.; Henke, M. Determination and Optimization of Multiphase Fractional-Slot Windings used in Permanent Magnet Synchronous Machines. In Proceedings of the 2021 24th International Conference on Electrical Machines and Systems (ICEMS), Gyeongju, Republic of Korea, 31 October–3 November 2021.
47. Li, W.; Cheng, M. Investigation of influence of winding structure on reliability of permanent magnet machines. *CES Trans. Electr. Mach. Syst.* **2020**, *4*, 87–95. [[CrossRef](#)]
48. Wang, S.; Zhu, Z.; Pride, A.; Shi, J.; Deodhar, R.; Umemura, C. Comparison of Different Winding Configurations for Dual Three-Phase Interior PM Machines in Electric Vehicles. *World Electr. Veh. J.* **2022**, *13*, 51. [[CrossRef](#)]
49. Beik, O.; Al-Adsani, A.S. *DC Wind Generation Systems: Design, Analysis, and Multiphase Turbine Technology*; Springer: Cham, Switzerland, 2020.
50. Yang, S.; Bryant, A.; Mawby, P.; Xiang, D.; Ran, L.; Tavner, P. An Industry-Based Survey of Reliability in Power Electronic Converters. *IEEE Trans. Ind. Appl.* **2011**, *47*, 1441–1451. [[CrossRef](#)]
51. Qin, B.; Liu, W.; Zhang, R.; Liu, J.; Li, H. Review on Short-circuit Current Analysis and Suppression Techniques for MMC-HVDC Transmission Systems. *Appl. Sci.* **2020**, *10*, 6769. [[CrossRef](#)]
52. High Power, High Frequency Transformers. Available online: <https://www.murata.com/en-us/products/transformers/highpower-highfrequency-transformers> (accessed on 10 March 2024).
53. Roth, M.E. *Evaluation of a Multi-Kw. High Frequency Transformer for Space Applications*; Lewis Research Center: Cleveland, OH, USA, 1994.
54. Optimization of Nuclear Fuel Assembly Loading Patterns. Available online: <https://quantumcomputinginc.com/optimization-of-nuclear-fuel-assembly-loading-patterns> (accessed on 10 March 2024).
55. Sarfi, G.; Beik, O. High Voltage Wind Turbine Conversion System with Dual DC Converter for MVDC Grids. In Proceedings of the 2023 IEEE Energy Conversion Congress and Exposition (ECCE), Nashville, TN, USA, 29 October–2 November 2023; pp. 563–567.
56. Khan, M.Y.A.; Liu, H.; Habib, S.; Khan, D.; Yuan, X. Design and Performance Evaluation of a Step-Up DC–DC Converter with Dual Loop Controllers for Two Stages Grid Connected PV Inverter. *Sustainability* **2022**, *14*, 811. [[CrossRef](#)]
57. Noruzi, S.; Ghoreishy, H.; Ahmad, A.A.; Tahami, F.; Ahmadihangar, R.; Rosin, A. Variable Frequency Control method of Boost Converter Operating in Boundary Conduction Mode. In Proceedings of the IEEE International Scientific Conference on Power and Electrical Engineering of Riga Technical University (RTUCON), Riga, Latvia, 5–7 November 2020; pp. 1–6.
58. Xiang, Y.; Chung, H.S.-H.; Lin, H. Light Implementation Scheme of ANN-Based Explicit Model-Predictive Control for DC–DC Power Converters. *IEEE Trans. Ind. Inform.* **2023**, *20*, 4065–4078. [[CrossRef](#)]

**Disclaimer/Publisher’s Note:** The statements, opinions and data contained in all publications are solely those of the individual author(s) and contributor(s) and not of MDPI and/or the editor(s). MDPI and/or the editor(s) disclaim responsibility for any injury to people or property resulting from any ideas, methods, instructions or products referred to in the content.